Supporting Information for

Gold(I) complexes with redox active BIAN and MIAN ligands: synthesis, structure and electrochemistry

Elena E. Bardina,[a] Nikita Y. Shmelev,[a] Yana N. Al'brekht,[a] Winnie Ka Yiu Koon,[b] Pavel A. Abramov,[a] Irina V. Mirzaeva,[a] Dmitriy G. Sheven',[a] Evgeniya V. Makotchenko,[a] Iakov S. Fomenko,[a] Anton N. Lukoyanov,[c] Maxim N. Sokolov,[a] Maria V. Babak,[b]* Artem L. Gushchin[a]*

[a] *Nikolaev Institute of Inorganic Chemistry SB RAS, 3 Acad. Lavrentiev Avenue, Novosibirsk, 630090, Russian Federation*

[b] *Drug Discovery Lab, Department of Chemistry, City University of Hong Kong, 83 Tat Chee Avenue, Hong Kong SAR, 999077, People's Republic of China*

[c] *Razuvaev Institute of Organometallic Chemistry, Russian Academy of Sciences, 49 Tropinina Street, Nizhny Novgorod, 603950, Russian Federation*

Table of contents

Figure S13. Electron density critical points and bond paths for cations **1-4** and $1e^-$ reduced cations **1** and **2**.

Figure S14. HOMO (top) and LUMO (down) for cations **1-4** and 1e reduced cations **1** and **2**.

Figure S15. ORTEP representation of $[(PPh_3)Au(L)]^+$ cations in **1-4**.

Table S1. Crystal data and structure refinement for **1-4**.

Cartesian atomic coordinates for model structures in .xyz format are supplied as .zip file.

Table S2. Composition of bonding orbitals (BD) of Au-P bond.

Table S3. Population of selected NBOs.

Table S4. Selected geometric parameters of optimized structures of 1e reduced cations **1** and **2**.

Table S5. Properties of selected bond critical points (BCPs) of 1e reduced cations **1** and **2**. $\rho(\mathbf{r}_{BCP})$ – electron density, $\Delta\rho(\mathbf{r}_{BCP})$ – Laplacian of electron density, $V(\mathbf{r}_{BCP})$ – potential energy density, $G(\mathbf{r}_{BCP})$ – kinetic energy density, $M(\mathbf{r}_{BCP})$ – metallicity [55].

Cell lines and culture conditions

Human cancer cell lines HT-29 (human colorectal carcinoma), MDA-MB-231 (human breast adenocarcinoma), and MRC-5 (human lung fibroblasts, non-cancerous) were obtained from ATCC. All cells were cultured in DMEM containing 10% FBS and 1% of Penicillin-Streptomycin (10,000 U/mL) and grown in tissue culture flasks (75 cm^2 and 25 cm^2, SPL Life sciences) at 37 °C in a humidified atmosphere of 95% air and 5% CO_2. All drug stock solutions were prepared in DMSO, and the final concentration in the medium did not exceed 1%, at which cell viability was not inhibited.

Inhibition of cell viability assay

The cytotoxicity of compounds was determined using the MTT colorimetric test. The cells were harvested from culture flasks by trypsinization and seeded into Cellstar 96-well microculture plates at the seeding density of 6000 cells per well (6×10^4 cells/mL). After the cells were allowed to resume exponential growth for 24 h, they were exposed to drugs at different concentrations in media for 72 h. The drugs were diluted in complete medium at the desired concentration and added to each well (100 µL) and serially diluted to other wells. After exposure for 72 h, the media was replaced with MTT in media (5 mg/mL, 100 µL/well) and incubated for additional 50 min. Subsequently, the medium was aspirated, and the purple formazan crystals formed in viable cells were dissolved in DMSO (100 µL/well). Optical densities were measured at 570 nm using the BioTek Synergy H1 microplate reader. The quantity of viable cells was expressed in terms of treated/control (T/C) values by comparison to untreated control cells, and 50% inhibitory concentrations (IC_{50}) were calculated from concentration−effect curves by interpolation. Evaluation was based on means from at least three independent experiments, each comprising three replicates per concentration level.

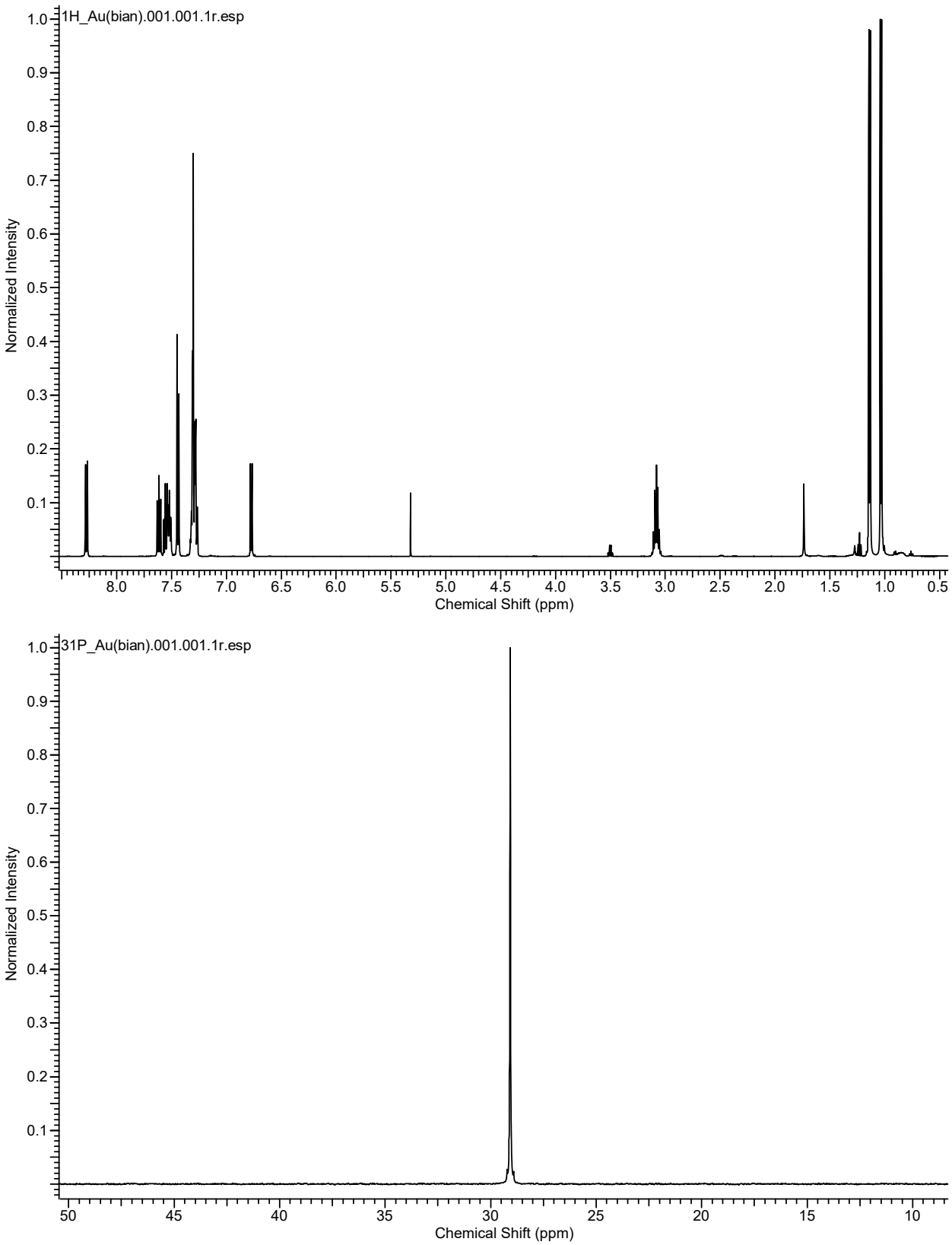

Figure S1. ^{1}H and $^{31}P\{^{1}H\}$ NMR spectra of **1** in $CDCl_3$.

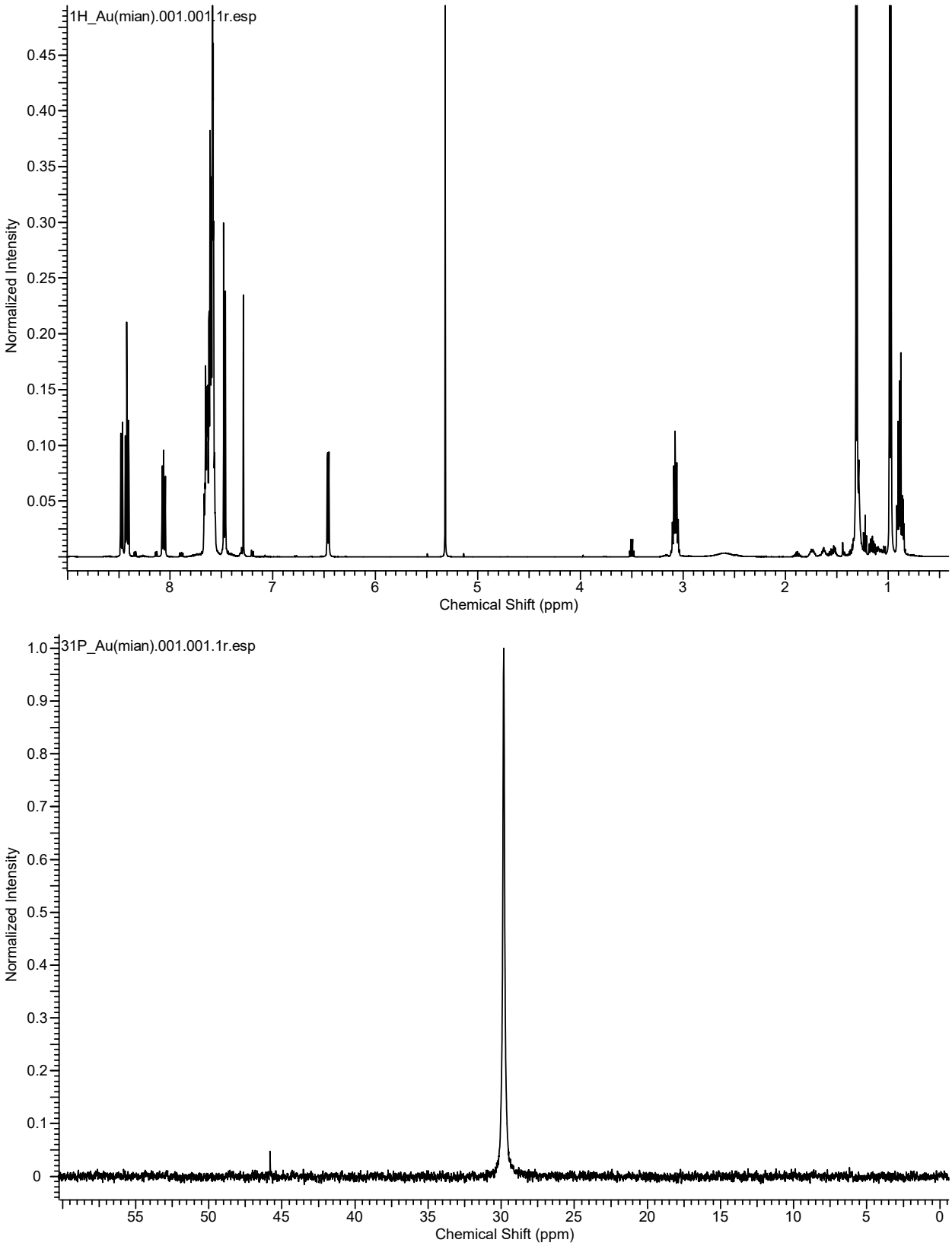

Figure S2. ^{1}H and $^{31}P\{^{1}H\}$ NMR spectra of **2** in $CDCl_3$.

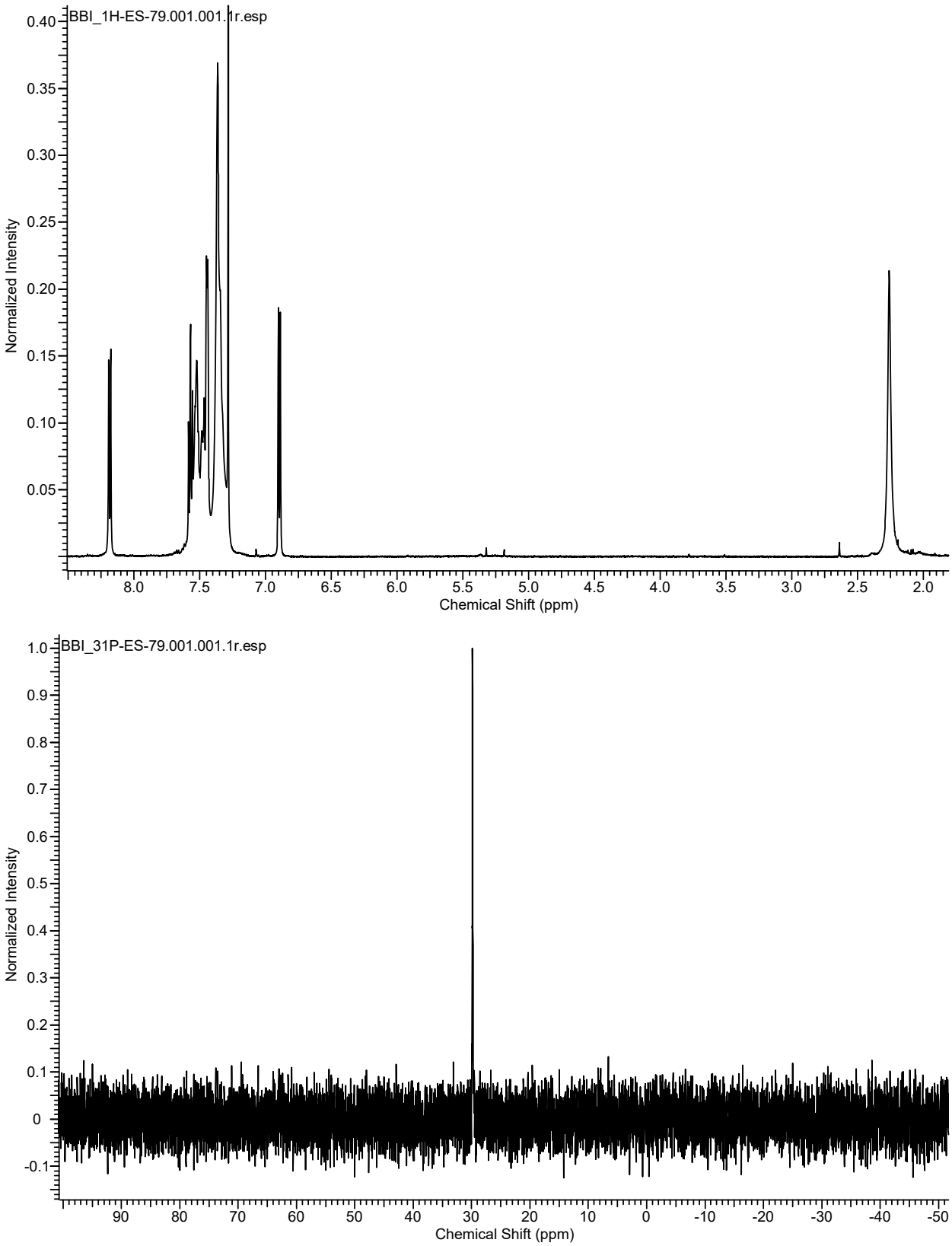

Figure S3. ^{1}H and $^{31}P\{^{1}H\}$ NMR spectra of **3** in $CDCl_3$.

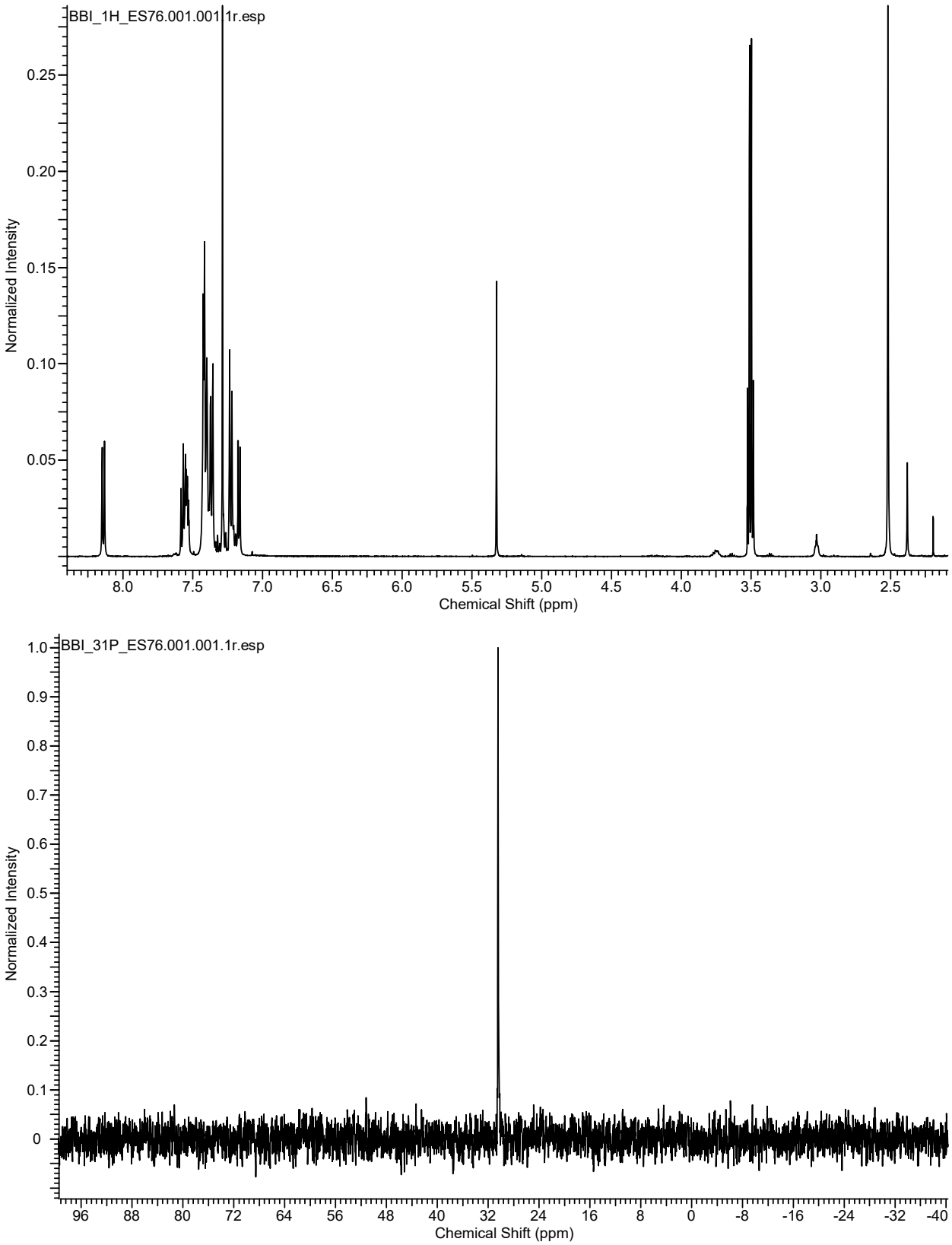

Figure S4. ^{1}H and $^{31}P\{^{1}H\}$ NMR spectra of **4** in $CDCl_3$.

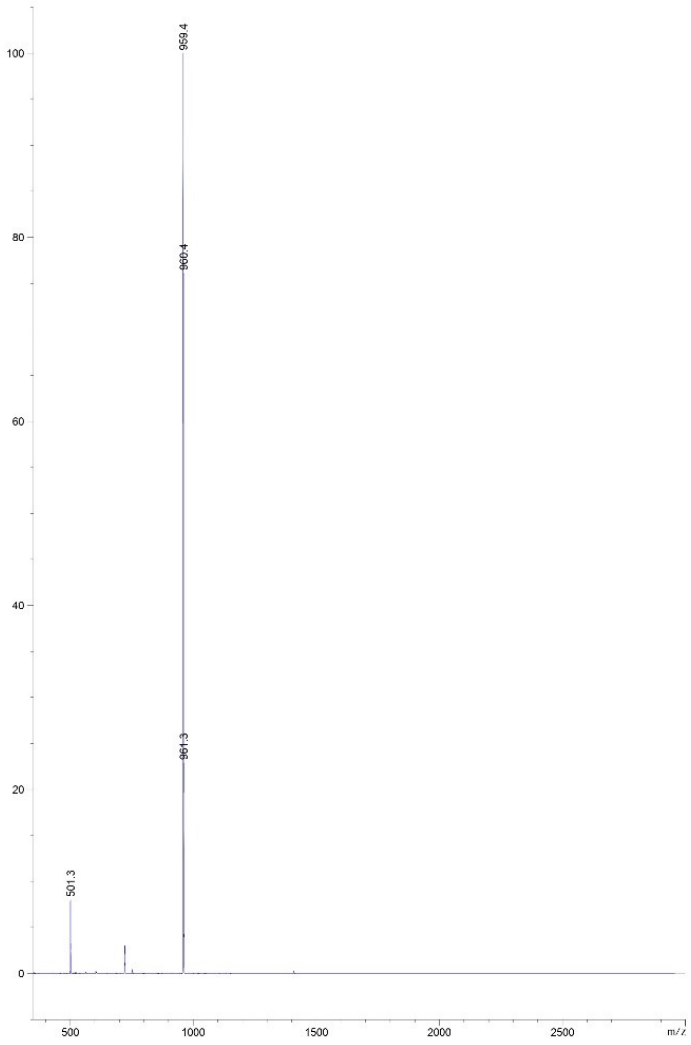

Figure S5. ESI-MS of **1** in CH_3CN.

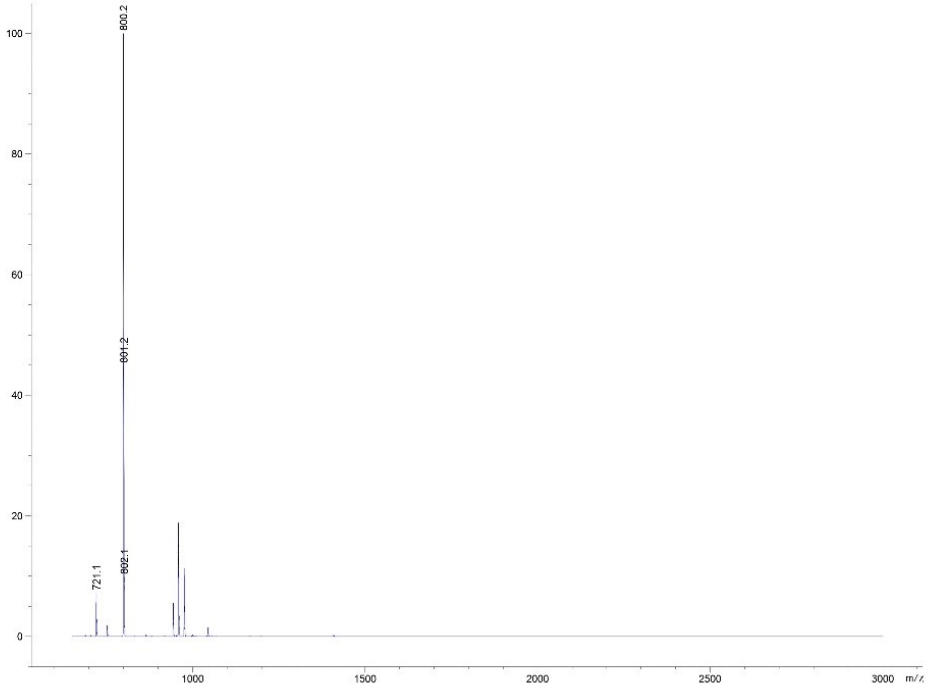

Figure S6. ESI-MS of **2** in CH_3CN.

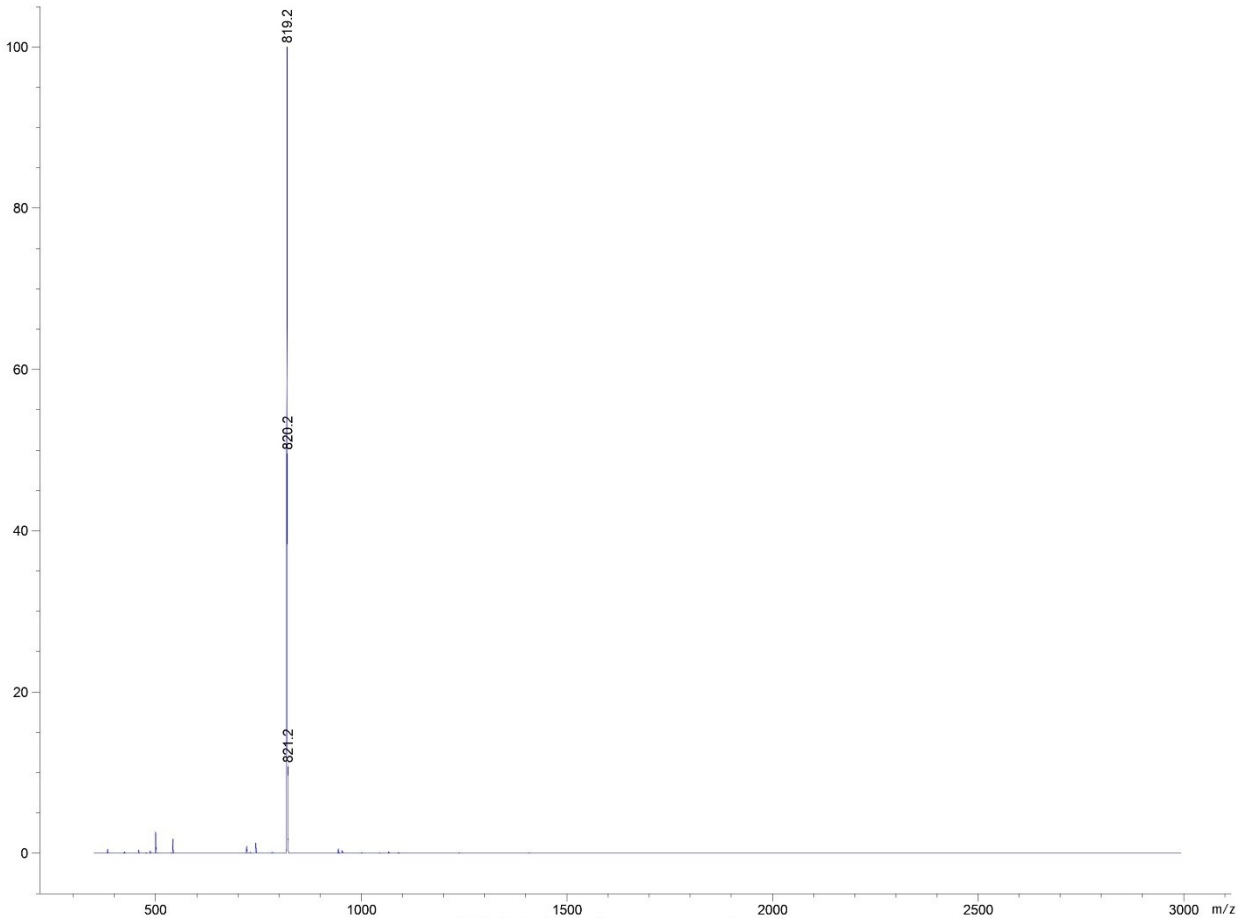

Figure S7. ESI-MS of **3** in CH_3CN.

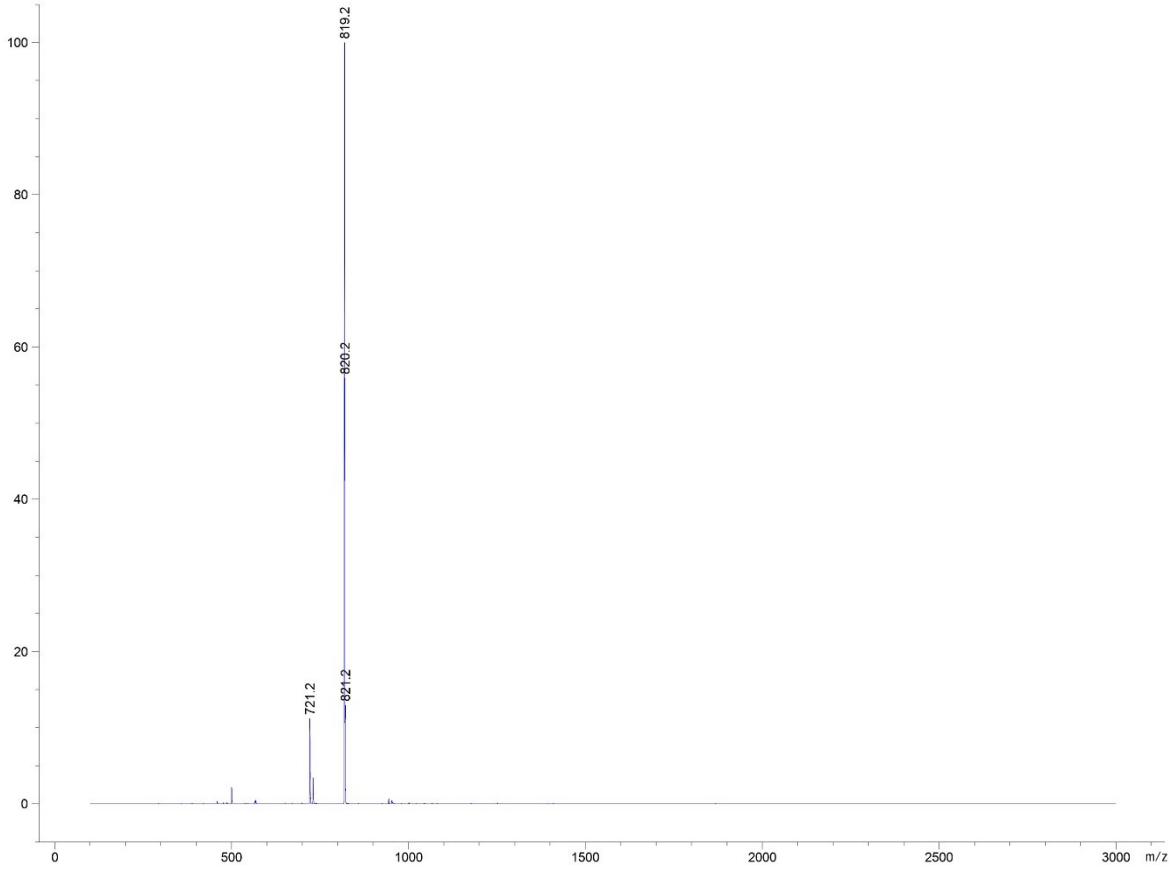

Figure S8. ESI-MS of **4** in CH_3CN.

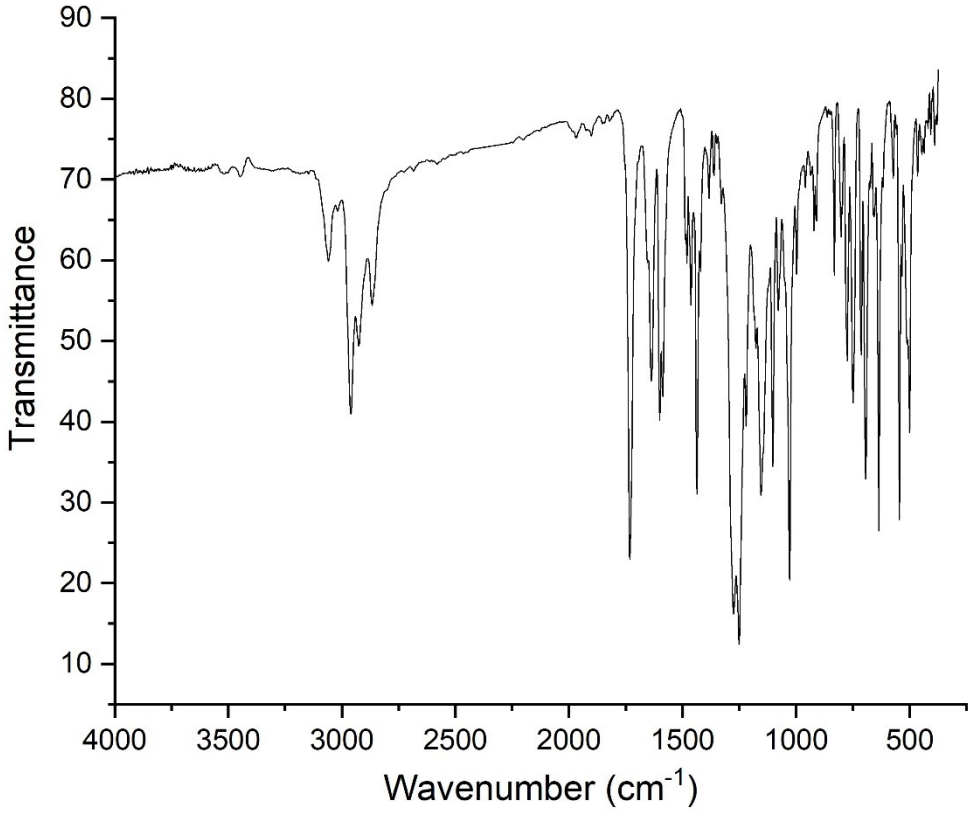

Figure S9. FT-IR spectrum of **2** in KBr.

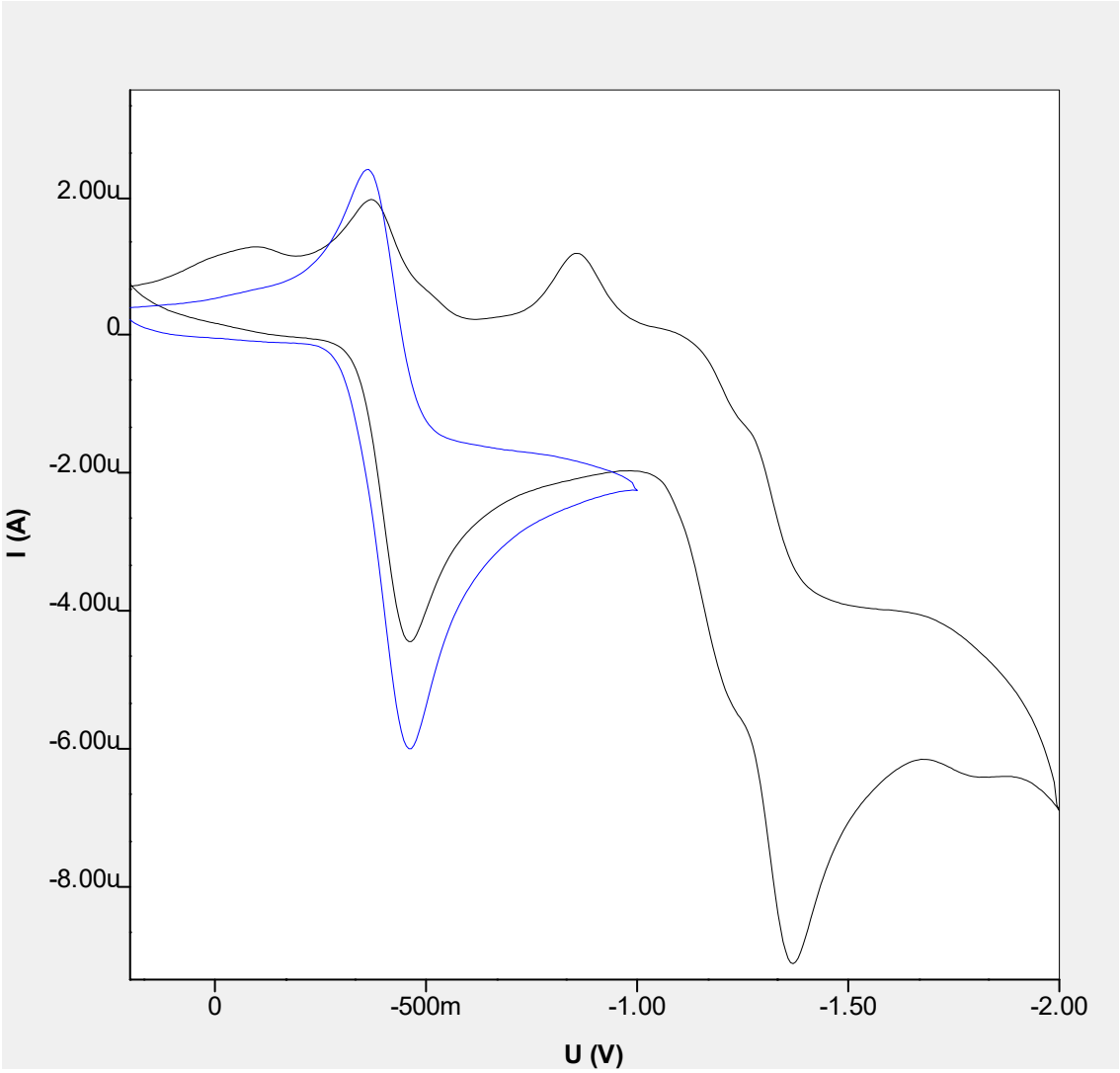

Figure S10. CV of **2** in CH_2Cl_2 at potential scan rate of 100 mV/s: grey spectrum – 0.2 ÷ -2.0 V region, blue spectrum – 0.2 ÷ -1.0 V region.

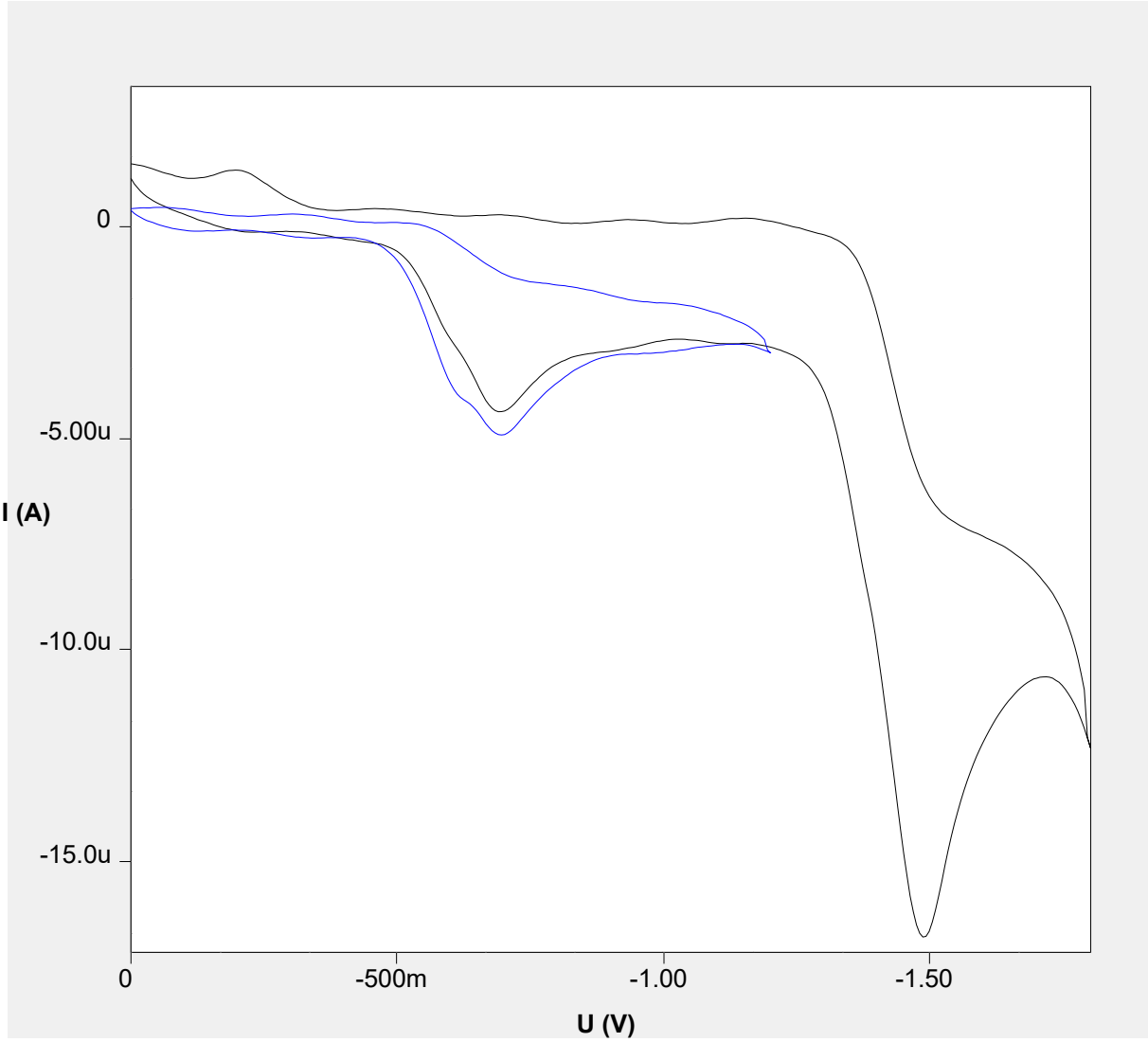

Figure S11. CV of **3** in CH_2Cl_2 at potential scan rate of 100 mV/s: grey spectrum – 0 ÷ -1.8 V region, blue spectrum – 0 ÷ -1.2 V region.

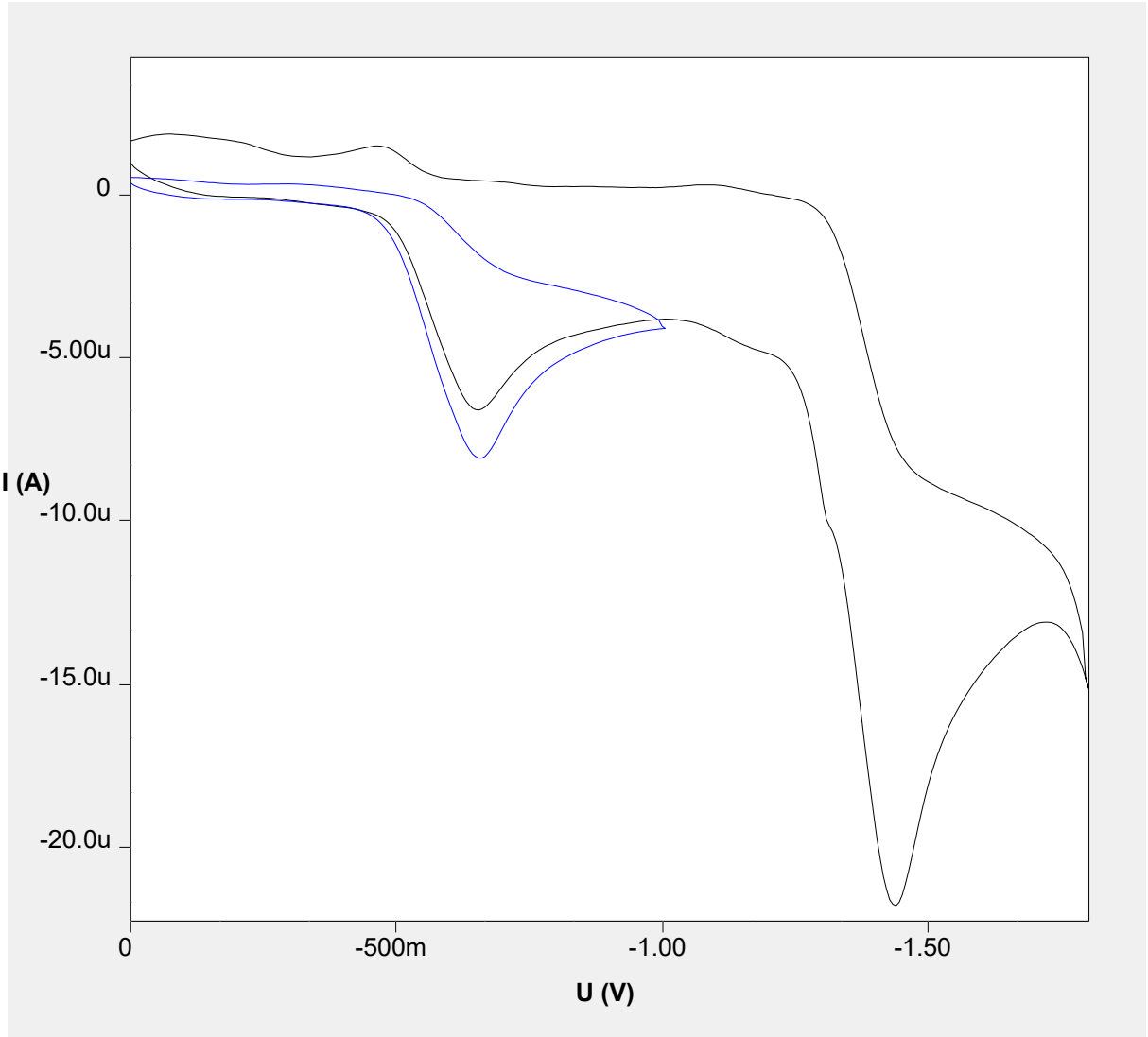

Figure S12. CV of **4** in CH_2Cl_2 at potential scan rate of 100 mV/s: grey spectrum – 0 ÷ -1.8 V region, blue spectrum – 0 ÷ -1.0 V region.

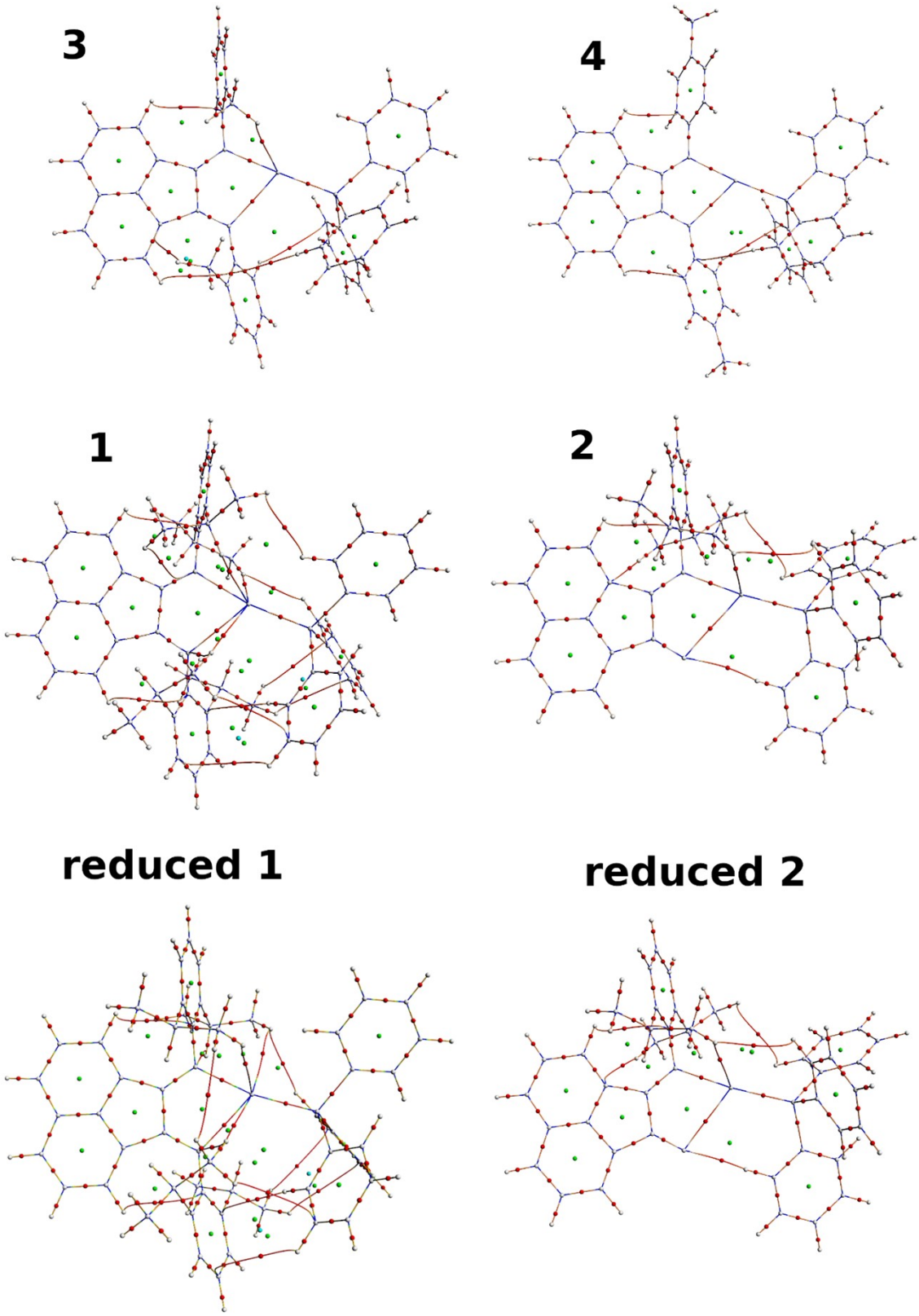

Figure S13. Electron density critical points and bond paths for cations **1-4** and $1e^-$ reduced cations **1** and **2**.

3

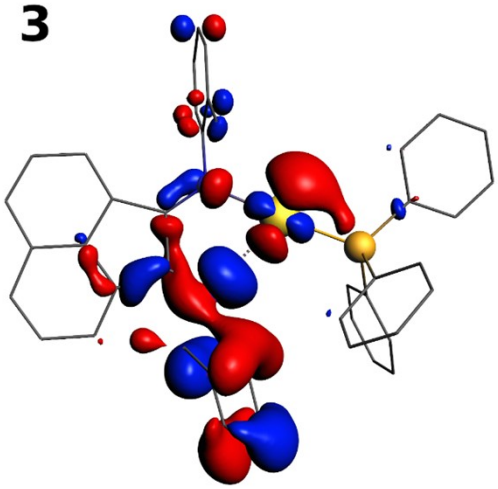

4

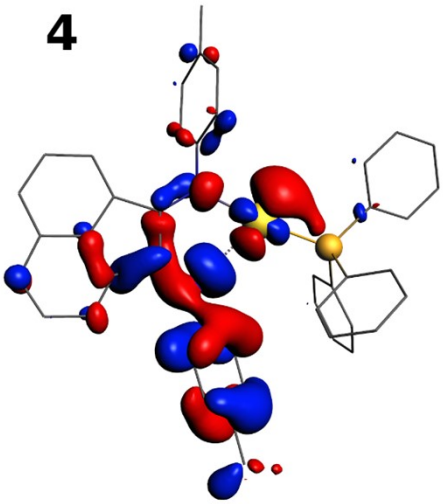

1

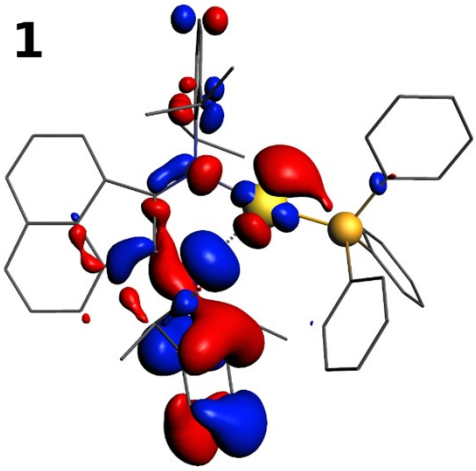

2

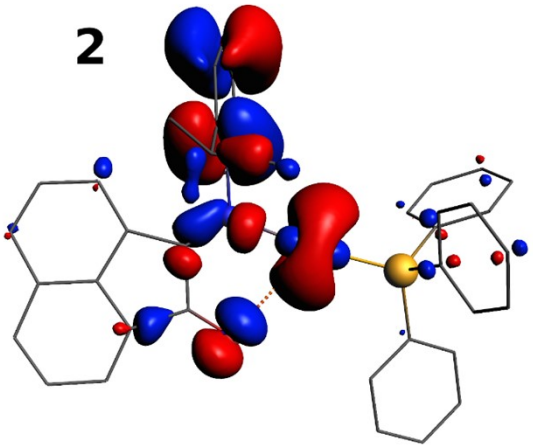

reduced 1

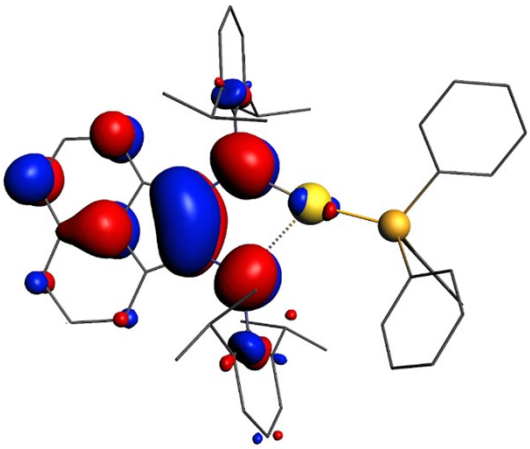

reduced 2

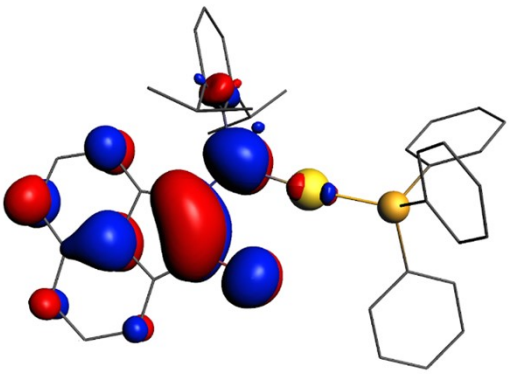

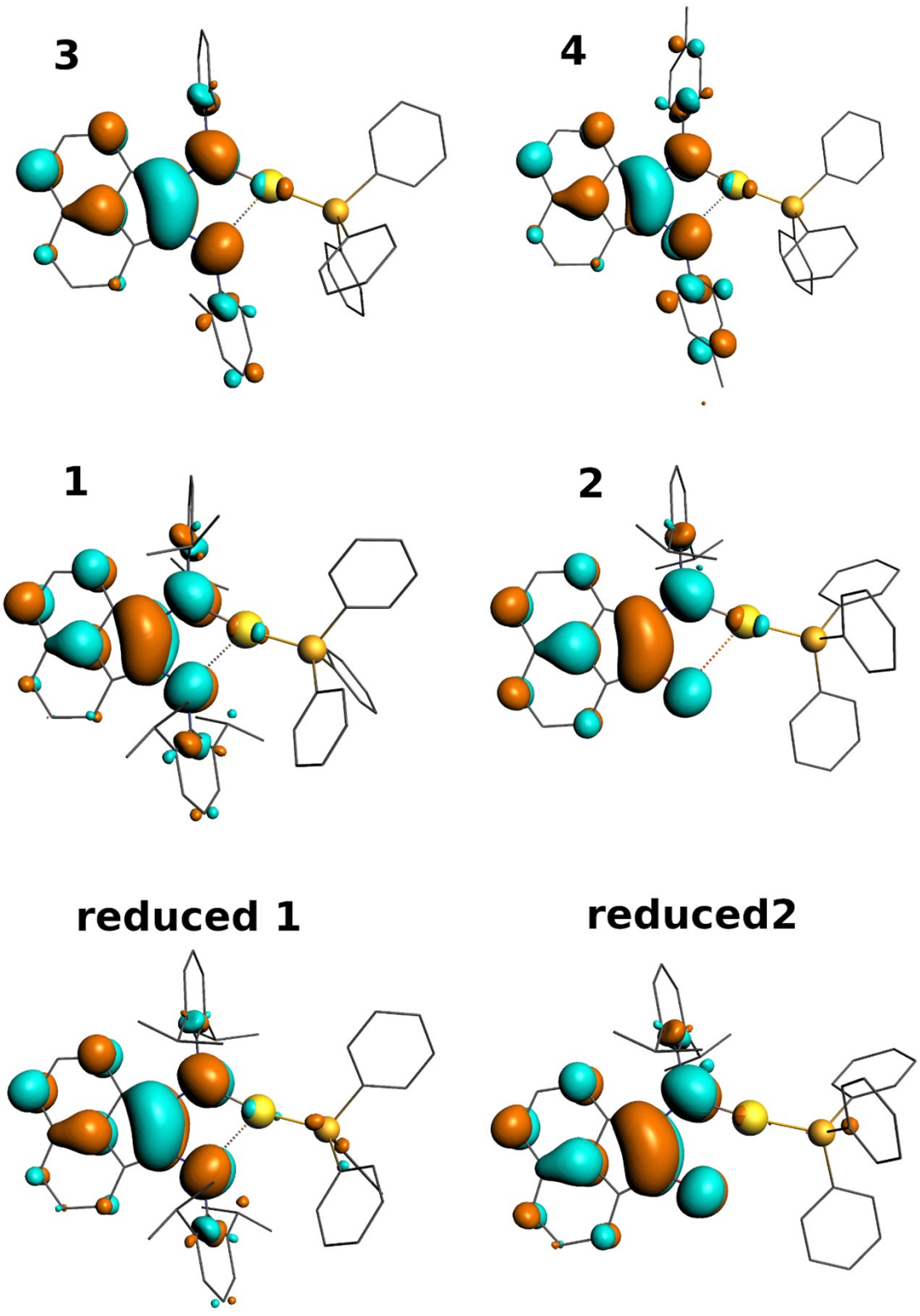

Figure S14. HOMO (top) and LUMO (down) for cations **1-4** and 1e reduced cations **1** and **2**.

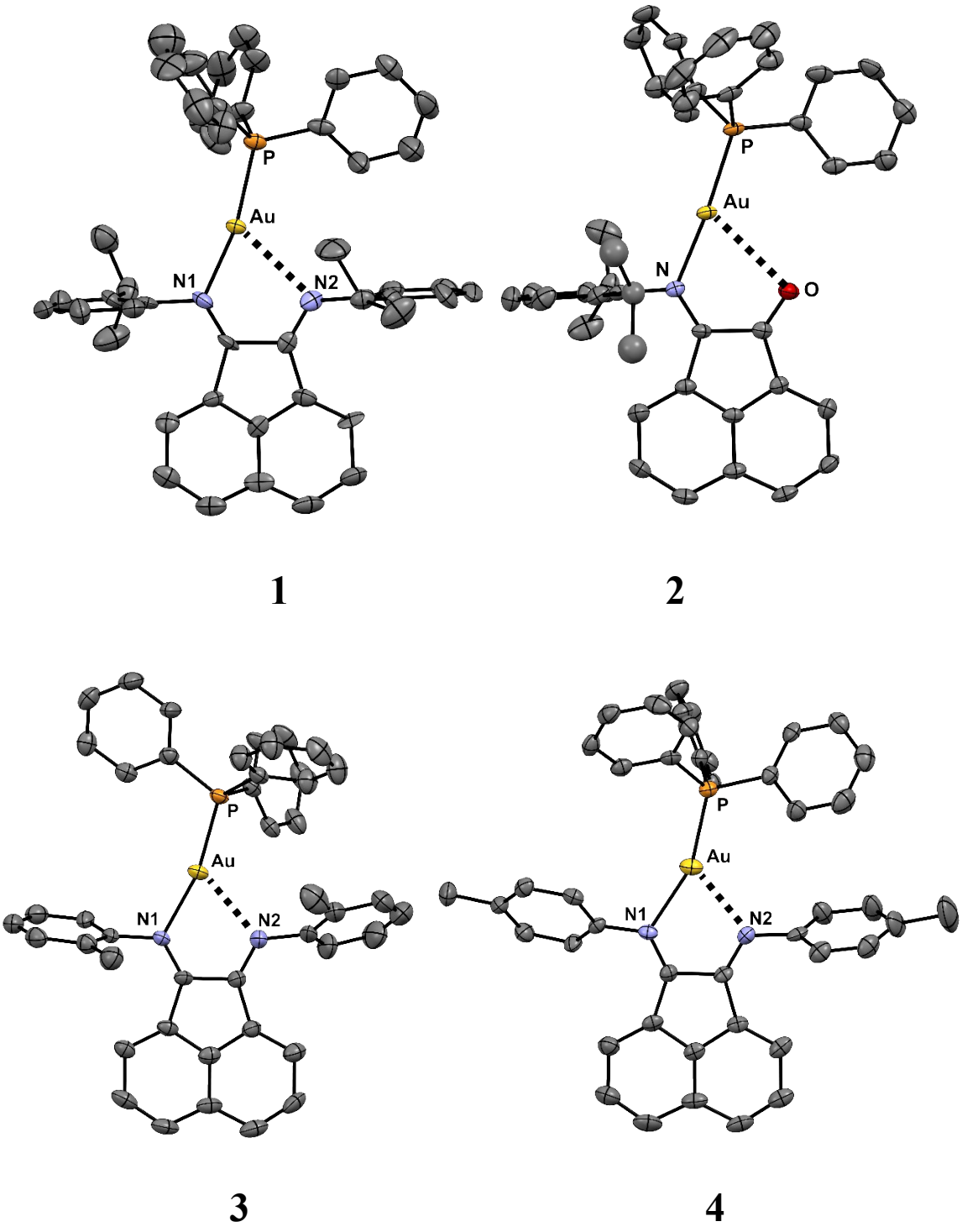

Figure S15. ORTEP representation of $[(PPh_3)Au(L)]^+$ cations in **1-4**.

Table S1. Crystal data and structure refinement for **1-4**.

	1	**2**	**3**	**4**
Chemical formula	$C_{54}H_{55}AuN_2P$	$C_{43.25}H_{38.50}AuCl_{0.50}F_3NO_4PS$	$C_{45}H_{35}AuF_3N_2O_3PS$	$C_{45.50}H_{36}AuClF_3N_2O_3PS$
M_r	959.93	970.97	968.74	1011.21
Crystal system, space group	Monoclinic, $P2_1/c$	Monoclinic, $P2_1/n$	Triclinic, $P\bar{1}$	Triclinic, $P\bar{1}$
a, b, c (Å)	18.2699 (6), 23.0750 (8), 23.4952 (8)	8.7066 (4), 15.2314 (10), 34.7368 (17)	10.3238 (4), 12.2164 (5), 17.0788 (8)	11.1358 (4), 11.5238 (5), 17.4708 (7)
α, β, γ (°)	90, 92.249 (1), 90	90, 95.214 (2), 90	92.890 (1), 96.360 (1), 114.033 (1)	104.247 (2), 95.590 (2), 104.326 (2)
V (Å^3)	9897.4 (6)	4587.5 (4)	1944.28 (14)	2075.31 (15)
Z	8	4	2	2
μ (mm^{-1})	3.04	3.37	3.94	3.75
Crystal size (mm)	0.16 × 0.10 × 0.05	0.58 × 0.38 × 0.07	0.04 × 0.03 × 0.02	0.05 × 0.03 × 0.01
Diffractometer	Bruker D8 Venture diffractometer	Bruker Apex Duo	Bruker D8 Venture diffractometer	Bruker D8 Venture diffractometer
Absorption correction	Multi-scan *SADABS* 2016/2: Krause, L., Herbst-Irmer, R., Sheldrick G.M. & Stalke D., J. Appl. Cryst. 48 (2015) 3-10	Multi-scan *SADABS* (Bruker-AXS, 2004)	Multi-scan *SADABS* 2016/2: Krause, L., Herbst-Irmer, R., Sheldrick G.M. & Stalke D., J. Appl. Cryst. 48 (2015) 3-10	Multi-scan *SADABS* 2016/2: Krause, L., Herbst-Irmer, R., Sheldrick G.M. & Stalke D., J. Appl. Cryst. 48 (2015) 3-10
T_{min}, T_{max}	0.635, 0.746	0.514, 0.746	0.586, 0.746	0.700, 0.746
No. of measured, independent and observed [$I > 2\sigma(I)$] reflections	118167, 24559, 18293	38203, 11704, 8885	22427, 8575, 6796	22348, 9049, 6839
R_{int}	0.067	0.044	0.049	0.063
$(\sin\theta/\lambda)_{max}$ (Å^{-1})	0.667	0.698	0.642	0.642
Range of h, k, l	h = -24→24, k = -30→26, l = -31→31	h = -12→12, k = -21→20, l = -45→45	h = -13→13, k = -15→15, l = -21→21	h = -14→14, k = -14→14, l = -22→22
$R[F^2 > 2\sigma(F^2)]$, $wR(F^2)$, S	0.036, 0.075, 1.00	0.047, 0.124, 1.06	0.043, 0.099, 0.96	0.054, 0.128, 1.01
No. of reflections	24559	11704	8575	9049
No. of parameters	989	501	507	534
No. of restraints	30	0	0	0
Weighting scheme	$w = 1/[\sigma^2(F_o^2) + (0.0286P)^2]$ where $P = (F_o^2 + 2F_c^2)/3$	$w = 1/[\sigma^2(F_o^2) + (0.0612P)^2 + 7.3863P]$ where $P = (F_o^2 + 2F_c^2)/3$	$w = 1/[\sigma^2(F_o^2) + (0.0547P)^2]$ where $P = (F_o^2 + 2F_c^2)/3$	$w = 1/[\sigma^2(F_o^2) + (0.0602P)^2]$ where $P = (F_o^2 + 2F_c^2)/3$
$\Delta\rangle_{max}$, $\Delta\rangle_{min}$ (e Å^{-3})	1.09, -0.75	1.47, -2.44	1.26, -1.65	1.82, -0.92

Computer programs: *APEX3* (Bruker-AXS, 2016), *APEX2* (Bruker-AXS, 2004), *SAINT* (Bruker-AXS, 2016), *SAINT* (Bruker-AXS, 2004), *SHELXS2014*/5 (Sheldrick, 2014), *SHELXT* 2014/5 (Sheldrick, 2014), *SHELXL2019*/3 (Sheldrick, 2019), *SHELXL2019*/2 (Sheldrick, 2019), *SHELXL2017*/1 (Sheldrick, 2017), ShelXle (Hübschle, 2011), CIFTAB-2014/2 (Sheldrick, 2014).

Table S2. Composition of bonding orbitals (BD) of Au-P bond.

1	(29.52%) Au s(87.47%) p(0.15%) d(12.37%) f(0.01%) (70.48%) P s(24.28%) p(75.44%) d(0.29%)
2	(30.67%) Au s(85.76%) p(0.14%) d(14.10%) f(0.01%) (69.33%) P s(23.64%) p(76.04%) d(0.32%)
3	(29.68%) Au s(86.66%) p(0.14%) d(13.19%) f(0.01%) (70.32%) P s(24.03%) p(75.68%) d(0.29%)
4	(29.31%) Au s(86.89%) p(0.14%) d(12.96%) f(0.01%) (70.69%) P s(24.24%) p(75.48%) d(0.28%)

Table S3. Population of selected NBOs.

	LP(N1)	LP(N2/O)	BD(Au-P)	BD*(Au-P)
1	1.73	1.81	1.94	0.26
2	1.72	1.84	1.94	0.26
3	1.72	1.82	1.94	0.26
4	1.72	1.83	1.94	0.26

Table S4. Selected geometric parameters of optimized structures of 1e reduced cations **1** and **2**.

	Au-P, Å	**Au-N1, Å**	**Au···N2/O, Å**	**<P-Au-N1, °**	**<P-Au…N2/O, °**
reduced 1	2.245	2.099	2.597	168.8	118.3
reduced 2	2.246	2.080	2.758	174.0	113.5

Table S5. Properties of selected bond critical points (BCPs) of 1e reduced cations **1** and **2**. $\rho(\mathbf{r}_{BCP})$ – electron density, $\Delta\rho(\mathbf{r}_{BCP})$ – Laplacian of electron density, $V(\mathbf{r}_{BCP})$ – potential energy density, $G(\mathbf{r}_{BCP})$ – kinetic energy density, $M(\mathbf{r}_{BCP})$ – metallicity [55].

Contact	Dist., Å	$\rho(\mathbf{r}_{BCP})$, a.u.	$\Delta\rho(\mathbf{r}_{BCP})$, a.u.	$V(\mathbf{r}_{BCP})$, a.u.	$G(\mathbf{r}_{BCP})$, a.u.	$M(\mathbf{r}_{BCP})$
reduced 1						
Au–N1	2.099	0.1074	0.3426	-0.1679	0.1268	4.88
Au···N2	2.597	0.0400	0.1230	-0.0371	0.0339	2.62
Au–P	2.245	0.1187	0.0910	-0.1723	0.0975	21.75
reduced 2						
Au–N1	2.080	0.1120	0.3559	-0.1791	0.1340	5.04
Au···O	2.758	0.0268	0.0904	-0.0213	0.0219	1.82
Au–P	2.246	0.1190	0.0895	-0.1728	0.0976	22.17